Monthly Notices
of the
ROYAL ASTRONOMICAL SOCIETY

MNRAS **515,** 99–109 (2022)
Advance Access publication 2022 June 21

https://doi.org/10.1093/mnras/stac1684

Experimental study of the removal of excited state phosphorus atoms by H_2O and H_2: implications for the formation of PO in stellar winds

Kevin M. Douglas,[1] David Gobrecht[2] and John M.C. Plane[1]★

[1]*School of Chemistry, University of Leeds, Leeds LS2 9JT, UK*
[2]*Department of Chemistry & Molecular Biology, University of Gothenburg, SE-40530 Göteborg, Sweden*

Accepted 2022 June 14. Received 2022 June 11; in original form 2022 April 27

ABSTRACT

The reactions of the low-lying metastable states of atomic phosphorus, P(^{2}D) and P(^{2}P), with H_2O and H_2 were studied by the pulsed laser photolysis at 248 nm of PCl_3, combined with laser-induced fluorescence detection of P(^{2}D), P(^{2}P), and PO. Rate coefficients between 291 and 740 K were measured, along with a yield for the production of PO from P(^{2}D or ^{2}P) + H_2O of (35 ± 15) %. H_2 reacts with both excited P states relatively efficiently; physical (i.e. collisional) quenching, rather than chemical reaction to produced PH + H, is shown to be the more likely pathway. A comprehensive phosphorus chemistry network is then developed using a combination of electronic structure theory calculations and a Master Equation treatment of reactions taking place over complex potential energy surfaces. The resulting model shows that at the high temperatures within two stellar radii of a MIRA variable AGB star in oxygen-rich conditions, collisional excitation of ground-state P(^{4}S) to P(^{2}D), followed by reaction with H_2O, is a significant pathway for producing PO (in addition to the reaction between P(^{4}S) and OH). The model also demonstrates that the PN fractional abundance in a steady (non-pulsating) outflow is underpredicted by about 2 orders of magnitude. However, under shocked conditions where sufficient thermal dissociation of N_2 occurs at temperatures above 4000 K, the resulting N atoms convert a substantial fraction of PO into PN.

Key words: astrochemistry – molecular data – methods: laboratory – stars: winds, outflows.

1 INTRODUCTION

The recent observations discussed below indicate that the PO/PN ratio around the oxygen-rich asymptotic giant branch (AGB) stars ranges from ∼1 to 20, and that the fractional abundances of PO and PN (i.e. with respect to the total gas which consists mostly of H_2, H, and He) are of the order of 10^{-8}–10^{-7}. De Beck et al. (2013) postulated that PO and PN are the main carriers of phosphorus in the gas phase, with abundances up to several 10^{-7}, since the solar elemental abundance of P is (2.6 ± 0.2) × 10^{-7} relative to H (Asplund et al. 2009). They also pointed out that chemical models could not account for these observations. For example, Gobrecht et al. (2016) modelled the chemistry around IK Tau, finding that PN was 6 × 10^{-7}; however, the modelled PO was severely depleted with a fractional abundance of only 2 × 10^{-10}.

Other recent observations of PO and PN around AGB stars include measured abundances of 1.7 × 10^{-6} and 7.3 × 10^{-7}, respectively, relative to H_2 in IK Tau (Velilla Prieto *et al.* 2017). Ziurys et al. (2018) reported peak abundances in the oxygen-rich circumstellar envelopes for several AGB stars of (0.5–1) × 10^{-7} and (1–2) × 10^{-8}, respectively, and concluded that the PO abundance is a factor of 5–20 greater than that of PN. This study suggests that phosphorus-bearing molecules are common in O-rich envelopes, and that a significant amount of phosphorus (>20 %) remains in the gas phase.

PO and PN have also been observed in star-forming regions. For example, Lefloch et al. (2016) showed that PN arises from the outflow cavity, where the strong shock tracer SiO is produced. Radiative transfer analysis indicated a PO/PN ratio of ∼3. The respective abundances of 2.5 × 10^{-9} and 0.9 × 10^{-9} imply a strong depletion, by approximately 2 orders of magnitude, of phosphorus in the quiescent cloud gas. This study also used shock modelling to demonstrate that atomic N plays a major role in the chemistry of PO and PN, concluding that the maximum temperature in the shock has to be larger than 4000 K. The production of these P-bearing species in shocks is supported by Fontani et al. (2019), who reported that the SiO and PN abundances are correlated over several orders of magnitude, and uncorrelated with gas temperature (which rules out alternative scenarios based on thermal evaporation from iced grain mantles). Mininni et al. (2018) found in a sample of nine massive dense cores that PN is well correlated with SiO in six out of the nine targets. However, in the other three objects, the PN lines do not exhibit high-velocity wings, indicating that PN can be formed in colder and more quiescent gas through alternative pathways. Most recently, Bernal et al. (2021) observed in the Orion-KL nebula a PO/PN ratio of ∼3, which is close to that measured in other warm molecular clouds. Finally, Rivilla et al. (2018) reported observations of PN and PO towards seven molecular clouds located in the Galactic Center. PN was detected in five out of the seven clouds whose chemistry appears to be shock dominated. The two clouds where PN was not detected are exposed to intense radiation (UV, X-rays, and cosmic rays). PO was detected only towards one cloud, with a PO/PN abundance ratio of ∼1.5.

★ E-mail: j.m.c.plane@leeds.ac.uk

© The Author(s) 2022.
Published by Oxford University Press on behalf of Royal Astronomical Society. This is an Open Access article distributed under the terms of the Creative Commons Attribution License (http://creativecommons.org/licenses/by/4.0/), which permits unrestricted reuse, distribution, and reproduction in any medium, provided the original work is properly cited.

Downloaded from https://academic.oup.com/mnras/article/515/1/99/6612737 by guest on 05 August 2022

In response to these observations, a number of modelling studies of P-bearing species have been published in the last three years. Jimenez-Serra et al. (2018) showed how the measured PO/PN ratio can be used to constrain the physical conditions and energetic processing of the P source. These workers proposed that the reaction P + OH → PO + H, which had not been considered previously, could be an efficient source of gas-phase PO. Chantzos et al. (2020) modelled the depletion level of P in diffuse and translucent clouds, followed by Sil et al. (2021), who used chemical models to explore the evolution of P-bearing species in various environments including diffuse clouds and hot cores. These workers noted a significant anticorrelation between the PO/PN ratio and atomic N, with a ratio < 1 in diffuse clouds where N is relatively high, and > 1 in hot core/corino regions.

Souza et al. (2021) pointed out that these models of phosphorus-bearing molecules such as PO rely on rate coefficients set to those of the analogous reactions of NO, which is not a satisfactory state of affairs given the importance of PO and PN in pre-biotic chemistry (Schwartz 2006, Walton et al. 2021). Souza et al. (2021) therefore employed accurate multireference configuration interaction calculations on the N + PO and O + PN reactions to explore their underlying mechanisms and calculate potential energy barriers. The results confirmed previous assumptions that depletion of PO by N atoms is fast, with a BR largely favouring O + PN rather than P + NO. Lastly, Molpeceres & Kästner (2021) published a theoretical study of the production of PH_3 on cold dust grains, resulting from the sequential addition of H atoms to adsorbed P.

In this paper, we first present the results of an experimental study of the following reactions over the temperature range of 291–740 K involving the two low-lying excited (metastable) states of atomic phosphorus, P(^{2}D) and P(^{2}P), with H_2O and H_2 (H_2O is, after H_2 and CO, the third most abundant molecule in oxygen-rich conditions, see e.g. Williams & Hartquist 2013):

		$\Delta H^\circ_{(0\,K)}$ (kJ mol^{-1})	
P(^{2}P) + H_2O	→ PO + H_2	–339	(R1a)
	→ P(^{2}D) + H_2O	–88	(R1b)
	→ P(^{4}S) + H_2O	–224	(R1c)
P(^{2}D) + H_2O	→ PO + H_2	–251	(R2a)
	→ P(^{4}S) + H_2O	–136	(R2b)
P(^{2}P) + H_2	→ PH + H	–81	(R3a)
	→ P(^{2}D) + H_2	–88	(R3b)
	→ P(^{4}S) + H_2	–224	(R3c)
P(^{2}D) + H_2	→ PH + H	+7	(R4a)
	→ P(^{4}S) + H_2	–136	(R4b)

where the reaction enthalpies (at 0 K) are calculated theoretically at the CBS-QB3 level of electronic structure theory (Montgomery et al. 2000). The role of P(^{2}D) and P(^{2}P), which are 1.41 and 2.32 eV, respectively above the P(^{4}S) ground state (Kramida et al. 2021), does not appear to have been considered previously in astrochemical models. However, our recent work on the P + O_2 reaction (Douglas et al. 2019), and the laboratory kinetics work described below (Section 3), shows that these metastable states are much more reactive than ground-state P(^{4}S). In order to develop a comprehensive chemical network for phosphorus, we then estimate the rate coefficients for other important reactions of P-containing species by combining electronic structure calculations with Rice–Ramsperger–Kassel–Markus statistical rate theory, using a Master Equation formalism. Finally, the revised and extended phosphorus chemical network is incorporated into a stellar outflow model with pulsations (shocks), to explore whether the new network can model satisfactorily the absolute PO and PN abundances, and the PO/PN ratio, around a MIRA variable AGB star.

2 EXPERIMENTAL METHODS AND NUMERICAL MODELLING

2.1 Reaction kinetics

The experimental apparatus employed in this study has been discussed in detail elsewhere (Gómez Martín *et al.* 2009, Douglas et al. 2019, Mangan et al. 2019, Douglas et al. 2020), so only a brief overview is given here. All experiments were conducted in a slow-flow reactor (residence time of the gas in the reactor ∼ 1 s) using the pulsed laser photolysis-laser-induced fluorescence (PLP-LIF) technique, with detection of either the first or second excited state of P (the ^{2}D and ^{2}P states, respectively, hereafter collectively referred to as P*), or PO. The reactor consists of a stainless-steel cell, with four horizontal side arms, orthogonally positioned, and a fifth vertical side arm. The cell is enclosed in a thermally insulated container, and can be operated at temperatures up to ∼1000 K. Temperatures inside the reactor are monitored by two K-type thermocouples, located towards the centre of the reactor volume. The phosphorus radical precursor (PCl_3), reagent gases, and bath gas were introduced into the chamber *via* four of the five side arms, after being combined in a mixing manifold to ensure homogenous mixing. PCl_3 was introduced as a dilute mixture (between 1 and 5 % in either N_2 or He), with concentrations of PCl_3 in the reaction chamber typically being ≤ 0.2 % of the total flow. Flow rates were controlled using calibrated mass flow controllers (MKS instruments), with total mass flow rates ranging from 100–400 standard cm^3 min^{-1}. These total flow rates are sufficient to ensure a fresh flow of gas through the interaction region for each photolysis laser pulse. The pressure inside the reactor, as measured by a calibrated capacitance manometer (Baratron MKS PR 4000), ranged from ∼3 to 11 Torr, and was controlled by a needle valve on the exit line to the pump. The photolysis and probe laser beams were introduced collinearly on opposite sides of the cell, and the fluorescence signal was collected using a photomultiplier tube (PMT) (Electron Tubes, model 9816QB) mounted orthogonally to the laser beams. To increase the solid angle of collected fluorescence, a glass tube of 1.5 cm diameter was positioned ∼1 cm above the interaction region to act as a waveguide for transporting fluorescence photons along the vertical side arm to the PMT.

P* atoms were produced from the multiphoton photolysis of PCl_3 at 248 nm (Douglas et al. 2019) using a KrF excimer laser (Lambda Physik COMPEX 102):

$$PCl_3 + nh\nu \rightarrow P\left(^2P\right), P\left(^2D\right) + \text{co–products}.$$

The excimer beam was loosely focused using a 50-cm focal length lens, with the focal point positioned approximately 10 cm beyond the interaction region, giving a beam cross-section of ∼8 mm^2 at the interaction region. Pulse energies at the interaction region ranged between 30 and 70 mJ pulse^{-1}. P* atoms were observed by time-resolved LIF spectroscopy, using the frequency-doubled output of an Nd:YAG pumped dye laser (a Quantel Q-smart 850 pumping a Sirah Cobra-Stretch with a BBO doubling crystal). The transitions and wavelengths employed are listed in Table 1. Resonance fluorescence

Downloaded from https://academic.oup.com/mnras/article/515/1/99/6612737 by guest on 05 August 2022

Table 1. Transitions used for laser-induced fluorescence detection of the first two excited states of P and of PO.

Radical Species	Excitation λ (nm)[a]	Transition	Laser dye	Filter[b]
$P(^2P)$[c]	255.3	$3s^23p^2(^3P)4\,s\ ^2P_{1/2} - 3s^23p^3\ ^2P^\circ_{1/2}$	Coumarin 503	254 (8)
$P(^2P)$[c]	253.6	$3s^23p^2(^3P)4\,s\ ^2P_{3/2} - 3s^23p^3\ ^2P^\circ_{3/2}$	Coumarin 503	254 (8)
$P(^2P)$[d]	215.4	$3s^23p^2(^1D)4\,s\ ^2D_{5/2} - 3s^23p^3\ ^2P^\circ_{3/2}$	Exalite 428	216 (10)
$P(^2P)$[d]	215.3	$3s^23p^2(^1D)4\,s\ ^2D_{3/2} - 3s^23p^3\ ^2P^\circ_{1/2}$	Exalite 428	216 (10)
$P(^2D)$	214.9	$3s^23p^2(^3P)4\,s\ ^2P_{1/2} - 3s^23p^3\ ^2D^\circ_{3/2}$	Exalite 428	216 (10)
$P(^2D)$	213.6	$3s^23p^2(^3P)4\,s\ ^2P_{3/2} - 3s^23p^3\ ^2D^\circ_{5/2}$	Exalite 428	216 (10)
PO	246.3	$A^2\Sigma^+ - X^2\Pi$ (v',v'' 0,0)[e]	Coumarin 503	254 (8)

[a]BBO frequency-doubling crystal employed. [b]Interference filter peak transmission wavelength (nm), FWHM in parentheses. [c]Transitions used to monitor loss of $P(^2P)$ with H_2 and H_2O. [d]Transitions used to compare LIF intensities with those of $P(^2D)$ lines. [e]$A^2\Sigma^+ - X^2\Pi$ (v', v'' 0,0) transition pumped at 246.3 nm and the non-resonant (v', v'' 0,1) LIF monitored at 255.4 nm (Sausa et al. 1986).

was measured by the PMT after passing through an appropriate interference filter (see Table 1), and recorded using a digital oscilloscope (LeCroy, LT262). The time-delay between probe and photolysis laser beams was varied to produce scans of the relative P* concentration with time. A typical time-resolved LIF profile (Fig. 2) consisted of 150 time-steps and resulted from the average of between 5 and 10 individual delay scans.

Two different methods were employed to introduce water vapour into the reaction cell. In the first, distilled H_2O was freeze-pump-thawed to remove volatile contaminants, and the subsequent H_2O vapour was diluted in a glass bulb (in either N_2 or He) on a glass vacuum line. The dilute H_2O vapour was then introduced to the chamber together with the other bath and precursor flows. For the second method, H_2O vapour was entrained within a flow of either N_2 or He passing through a glass bubbler (a modified Dreschel bottle) containing distilled H_2O. The bubbler, which was maintained at a constant temperature using a water bath, was located before the relevant mass flow controller, and the gas flow exiting the bubbler was shown to be saturated using a humidity probe (Process Sensing Technologies, PCMini52). The temperature of the bubbler was close to, or slightly below, room temperature. By measuring the temperature of the bubbler and the pressure of the N_2/He gas over the H_2O, the concentration of the H_2O entrained in the gas flow was determined *via* its known vapour pressure (Bridgeman & Aldrich 1964). The rate coefficients measured with these two methods for introducing H_2O vapour into the reaction cell were in good agreement (within 7 % at 300 K and 3 % at 390 K); in practice, the second method was mostly used. When studying R1 and R2, the H_2O gas flow was used to condition the reactor for 30 min prior to each experiment, to ensure that significant H_2O vapour was not lost to the reactor walls during the kinetic measurements.

2.2 PO product yields

Experiments to determine the PO product yields from reactions R1 and R2 were carried out using the same slow-flow reactor and PLP–LIF technique describe above. PO was produced from the reaction of P* with H_2O (R1a and R2a), and from the reaction of P* with any residual O_2 (R6a and R7a) in the reaction cell. P* atoms were produced *via* multiphoton photolysis of PCl_3 as described above, and PO was monitored by time-resolved LIF spectroscopy using the PO($A^2\Sigma^+ - X^2\Pi$) transition (see Table 1). PO yields were determined by monitoring the amount of PO produced from reactions R1a and R2a as a function of $[H_2O]$.

$P(^2P) + O_2$	$\rightarrow PO + O$	– 324	(R6a)
	$\rightarrow P(^2D) + O_2$	– 88	(R6b)
	$\rightarrow P(^4S) + O_2$	–224	(R6c)
$P(^2D) + O_2$	$\rightarrow PO + O$	–236	(R7a)
	$\rightarrow P(^4S) + O_2$	–136	(R7b)

To estimate the relative amounts of $P(^2D)$ and $P(^2P)$ produced following multiphoton photolysis of PCl_3 (for a particular precursor concentration and photolysis energy), the relative intensities of the LIF signal for the transitions in the 213.6–215.4 nm range were compared. As more ^2D than ^2P was produced in the multiphoton photolysis of PCl_3 (see Section 3.2), and as the ^2D state is efficiently relaxed by N_2 (Douglas et al. 2019), it was possible to tune the experimental conditions so that we were able to monitor PO produced primarily from either the $P(^2D)$ or the $P(^2P)$ state. For example, in experiments using N_2 as the bath gas, the high $[N_2]$ meant that the majority of $P(^2D)$ produced was removed by N_2 rather than by H_2O (or O_2). Thus, as the $P(^2P)$ state is not efficiently relaxed by N_2 (Douglas et al. 2019), the majority of PO observed results from $P(^2P)$ reacting with H_2O (or O_2), rather than $P(^2D)$. Conversely, in experiments using He as the bath gas, the majority of $P(^2D)$ produced was now removed by H_2O. As more $P(^2D)$ was produced in our experiments than $P(^2P)$, it is likely that the majority of PO observed was from the reaction of $P(^2D)$ with H_2O rather than $P(^2P)$. As such, experiments measuring PO yields were carried out either using N_2 or He as the bath gas. For each bath gas, three or four sets of product yields were collected, over an $[H_2O]$ range of 0–1 $\times$ 10^{16} molecule cm^{-3} and 0–6 $\times$ 10^{15} molecule cm^{-3} for experiments in N_2 and He, respectively.

In experiments measuring the PO product yields, the recorded PO fluorescence signals were corrected for the quenching of the PO($A^2\Sigma^+$) by H_2O. This was done by determining the PO($A^2\Sigma^+$) fluorescence rate coefficient, k_f, as a function of $[H_2O]$. Using an oscilloscope, 100 fluorescence decays were averaged, and then fitted using an exponential function (Fig. 1):

$$I_t = I_{f0} \,.\, \exp^{(-k_f.t)} \quad (1)$$

By looking at the ratio of the fluorescence lifetime at a particular $[H_2O]$ compared to that with no H_2O present, a correction factor, S, could be obtained, and applied to the absolute PO fluorescence signals obtained:

$$S = k_{f([H_2O]} \,/\, k_{f(H_2O\,=\,0)}. \quad (2)$$

Downloaded from https://academic.oup.com/mnras/article/515/1/99/6612737 by guest on 05 August 2022

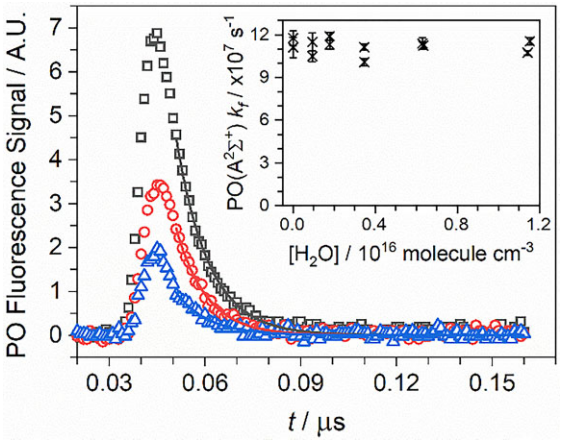

Figure 1. PO($A^2\Sigma^+$) fluorescence signal captured from the oscilloscope from experiments using N_2 as a bath gas, at three [H_2O]: black squares [H_2O] = 1.8×10^{16} molecule cm^{-3}; red circles [H_2O] = 1.1×10^{16} molecule cm^{-3}; blue triangles [H_2O] = 0×10^{16} molecule cm^{-3}. The solid lines are single exponential fits to each signal decay; these fits start far enough in time after the respective peaks in the bi-exponential signal that the early fast growth has ended. Inset panel: PO($A^2\Sigma^+$) fluorescence lifetime, k_f, *vs* [H_2O], from experiments using N_2 as a bath gas.

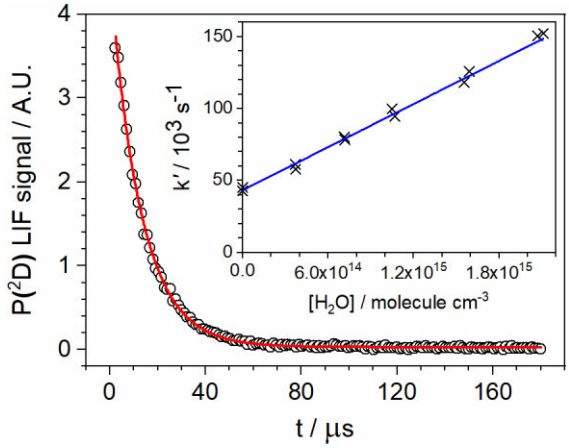

Figure 2. P(^{2}D) LIF signal following PLP of PCl_3 at a total pressure of 7.64 Torr and [H_2O] = 7.19×10^{14} molecule cm^{-3}, at $T = 593$ K. Inset panel: a bimolecular plot for reaction R2 at $T = 593$ K, giving $k_2 = (4.99 \pm 0.30) \times 10^{-11}$ cm^3 $molecule^{-1}$ s^{-1}.

In practice, k_f was shown to be effectively independent of [H_2O] in all experiments (inset to Fig. 1), suggesting that quenching of the PO($A^2\Sigma^+$) signal was essentially all from the N_2 or He bath gas. The absolute PO LIF signals were therefore not corrected for H_2O quenching.

2.3 Materials

He [99.9995 %, British Oxygen Company (BOC)], N_2 (99.9995 %, BOC), and H_2 (99.99 %, BOC) were used without further purification. PCl_3 (≥ 99.0 %, VWR International Ltd.) and deionized H_2O were initially degassed by freeze-pump-thawing to remove volatile contaminants, and then made up as dilute vapours in N_2 or He.

3 RESULTS

3.1 P* + H_2O and H_2 removal rates

An example of the time-resolved LIF signal for P(^{2}D) in the presence of H_2O can be seen in Fig. 2. The LIF signal for both P(^{2}D) and P(^{2}P) decayed exponentially with time, with no increase in the LIF signal observed even at very short probe-photolysis delay times. As all experiments were carried out under pseudo-first-order conditions (i.e. [P*] << [H_2O] or [H_2]), the loss of P* can be described by a single exponential of the form:

$$[P^*]_t = [P^*]_0 .\exp^{(-k'.\,t)}, \quad (3)$$

where $[P^*]_0$ is the initial concentration of P* from photolysis of PCl_3, t is the time-delay between the probe and photolysis laser pulses, and k' is the experimentally observed pseudo-first-order loss rate, which is equal to

$$k' = k_r\,.\,[R] + k'_{diff} \quad (4)$$

This expression encompasses the rates for all losses of P*, including diffusion and removal by the bath and precursor gases (summed as k'_{diff}), and removal by the co-reagent, R. Equation E3 was fitted to the P* profiles to extract the parameters $[P^*]_0$ and k' (Fig. 2). Plotting k' *vs* [R] then yields a straight line with a gradient equal to the bimolecular rate constant, k_r, and the intercept equal to k'_{diff} (inset Fig. 2).

The bimolecular rate coefficients for the removal of P* with H_2O and H_2 are presented as a function of temperature in Fig. 3, and listed in Table S1 in the Supporting Information (SI). Errors are reported at the 1σ level for the linear least-squares fitting of the pseudo-first order coefficients as a function of co-reagent concentration. The temperature range over which reactions R1–R4 could be studied was limited by thermal decomposition in our reaction cell of the PCl_3 precursor at temperatures higher than ∼750 K. No effects were observed on the bimolecular rate coefficients determined in this study when the PCl_3 precursor concentration and photolysis energy were varied by around a factor of 2, or when using different probe wavelengths. Varying the total pressure by around a factor of 3 also had no effect on the rate coefficients determined at room temperature.

There has only been one previous study investigating the removal of P* with H_2, with only a room temperature value reported (Acuña et al. 1973). In their study, P* was produced by single-photon pulsed photolysis of PCl_3 at VUV wavelengths ($\lambda < 160$ nm), while removal of P* was observed using time-resolved atomic resonance absorption spectroscopy. As can be seen from Fig. 3 and Table 1, the room temperature result for P(^{2}P) + H_2 reported by Acuña et al. (1973) is around 70 % larger than our value, with the two values lying just outside their mutual error limits. For P(^{2}D) + H_2, our room temperature value is around 80 % larger than that reported by Acuña et al. (1973). We reported a similar discrepancy between our room temperature values for the removal of P(^{2}D) with O_2 and CO_2 (Douglas et al. 2019), with our values being around 50 and 80 % faster, respectively, than those reported by Acuña et al. (1973). We are unable to account for these discrepancies; however, it should be noted that we obtain consistent room temperature values over a range of pressures, precursor concentrations, and photolysis energies, using two different probe wavelengths. Looking at the temperature dependence of P* + H_2, we see typical Arrhenius behaviour for both the P(^{2}P) and P(^{2}D) states, with a small positive temperature dependence, which can be parametrized as follows (see solid lines in Figs 3a and b; units: cm^3 $molecule^{-1}$ s^{-1}, 1σ errors):

Downloaded from https://academic.oup.com/mnras/article/515/1/99/6612737 by guest on 05 August 2022

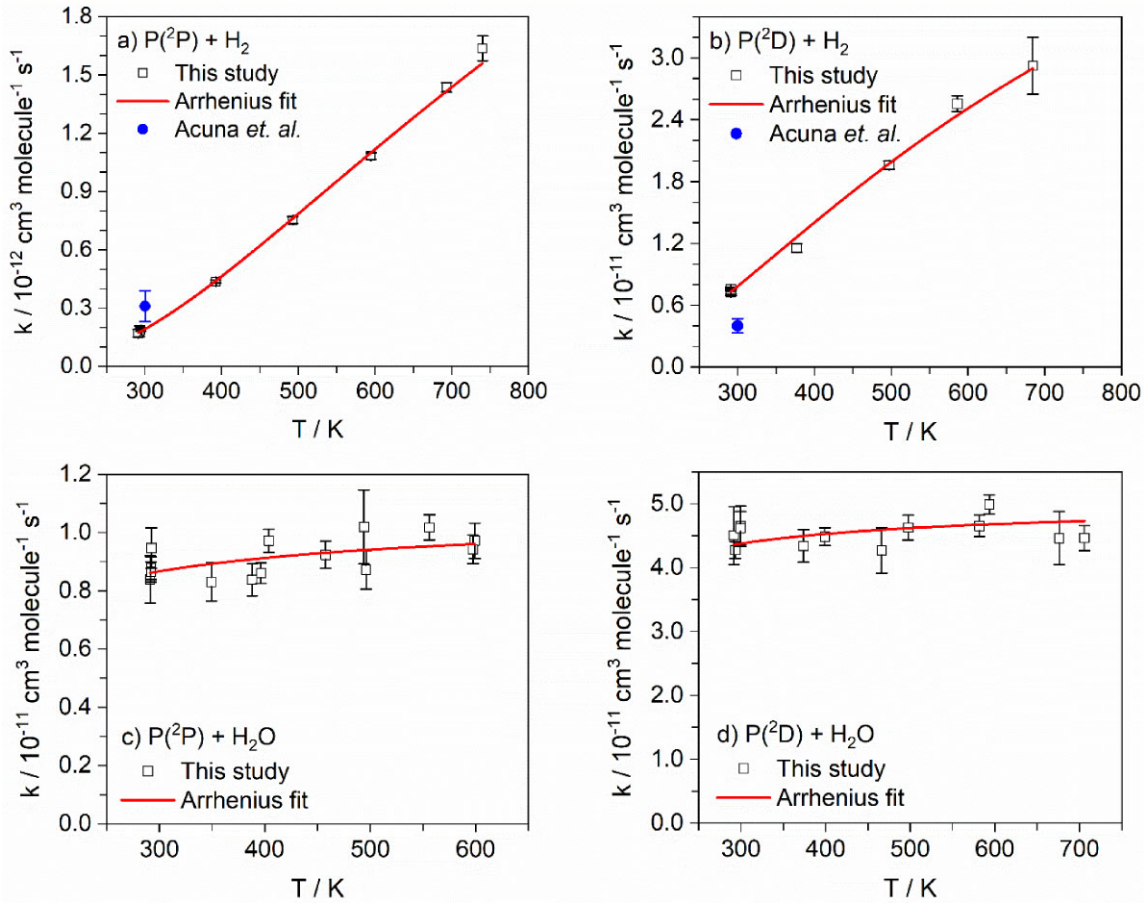

Figure 3. Temperature dependence of the rate coefficient for Panel (a): $P(^2P) + H_2$, Panel (b): $P(^2D) + H_2$, Panel (c): $P(^2P) + H_2O$, and Panel (d): $P(^2D) + H_2O$. Black open squares are from this study, with Arrhenius fits indicated by red lines; solid blue circles are from Acuña et al. (1973).

$$k_{(P(^2P)+\,H_2)}\,(291 \le T/K \le 740) = (6.50 \pm 0.18) \times 10^{-12} \exp^{[(-1056\pm14)/T]},$$

$$k_{(P(^2D)+H_2)}\,(291 \le T/K \le 684) = (8.04 \pm 0.48) \times 10^{-11} \exp^{[(-699\pm22)/T]}.$$

There appear to have been no previous studies of the removal of P^* with H_2O. As can be seen from Fig. 3 and Table S1, the removal of both $P(^2P)$ and $P(^2D)$ by H_2O shows only a weak temperature dependence between 300 and 700 K, and might effectively be temperature independent within error; this is in contrast to the removal of P^* with other collision partners such as O_2, H_2, CO_2, and N_2, all of which show a moderate positive temperature dependence above 300 K (Douglas et al. 2019). Parameterization of the rate coefficients for $P^* + H_2O$ over the experimental temperature range yields (see solid lines in Figs 3c and d; units: cm^3 $molecule^{-1}$ s^{-1}, 1σ errors):

$$k_{(P(^2P)+H_2O)}\,(291 \le T/K \le 599) = (1.06 \pm 0.06) \times 10^{-13} \exp^{[(-62\pm23)/T]},$$

$$k_{(P(^2D)+H_2O)}\,(292 \le T/K \le 706) = (5.01 \pm 0.22) \times 10^{-12} \exp^{[(-40\pm17)/T]}.$$

3.2 PO yields

PO LIF profiles produced following the multiphoton photolysis of PCl_3 in the presence of H_2O are shown in Fig. 4. Because the experiments were carried out under pseudo-first-order conditions (i.e. $[P^*] << [H_2O]$ and $[O_2]$), the growth and loss of the PO signal can be described by a bi-exponential function of the form:

$$[PO]_t = \gamma \left(\frac{k'_{growth}}{k'_{loss} - k'_{growth}} \right) [P^*]_0 \left(\exp^{-k'_{growth} \cdot t} - \exp^{-k'_{loss} \cdot t} \right), \quad (5)$$

where k'_{growth} and k'_{loss} are the pseudo-first-order rate coefficients for the reactions producing and removing PO, and $[P^*]_0$ is the amount of P^* formed following multiphoton photolysis of the PCl_3 precursor, and γ is the observed yield for PO production (as opposed to physical quenching). As PO itself does not react with H_2O, it is primarily lost through reaction with residual O_2 (R8):

$$PO + O_2 \rightarrow PO_2 + O \quad (R8)$$

Although the PO profiles are not strictly biexponential in nature, as the growth of the PO signal is from the reaction of two different species, they could be satisfactorily fit using equation E5 (see Fig. 4), and the parameters k'_{growth}, k'_{loss}, and γ extracted.

The PO yields obtained are plotted as a function of $[H_2O]$ in Fig. 5. Because of day-to-day variations in the efficiency of the LIF collection system and power of the photolysis laser, the absolute PO yields collected under the same experimental conditions differed slightly. In order for them to be directly comparable to one another,

Downloaded from https://academic.oup.com/mnras/article/515/1/99/6612737 by guest on 05 August 2022

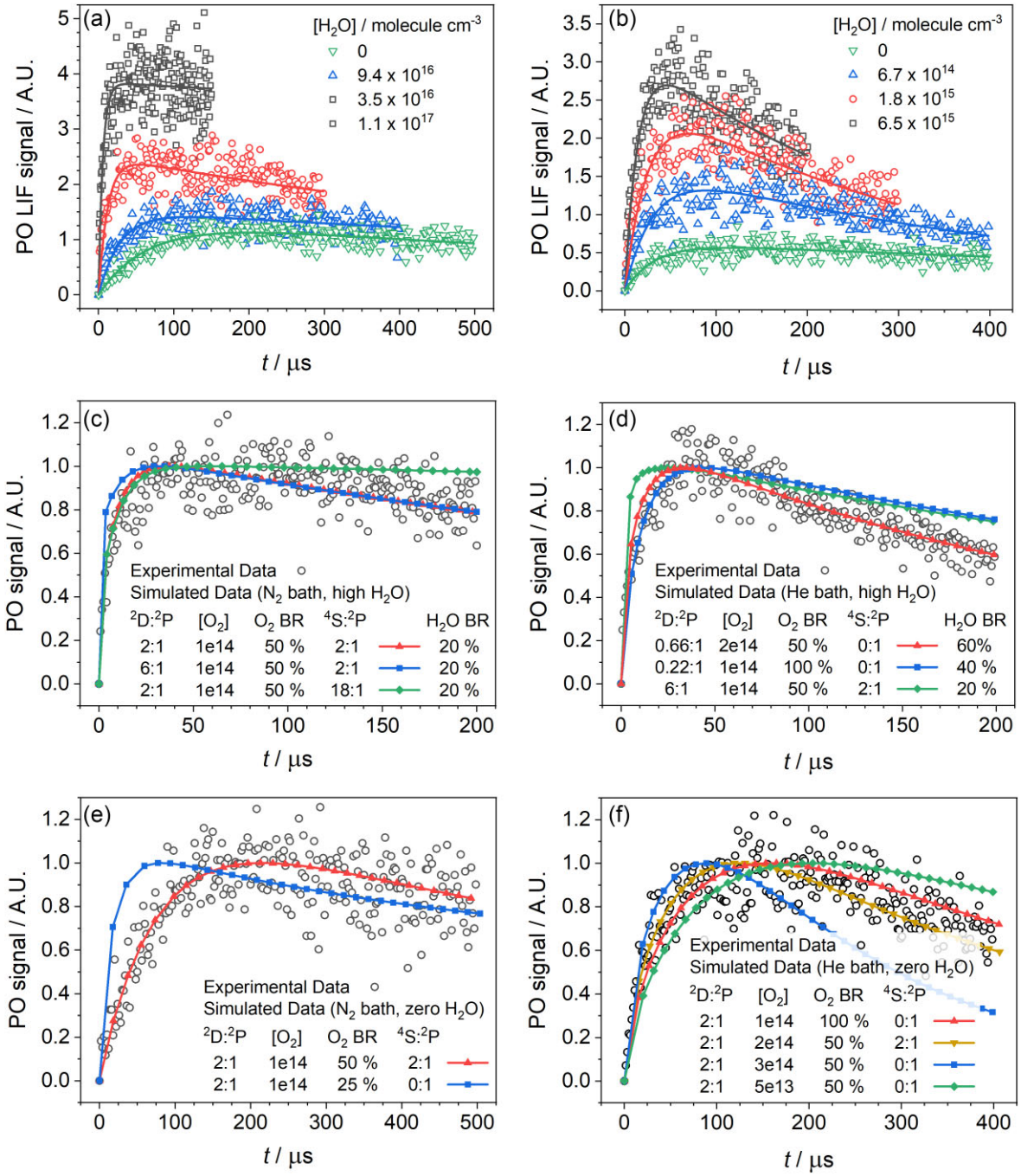

Figure 4. Top panels: PO LIF signals following PLP of PCl_3 at various $[H_2O]$. Solid lines are fits of Equation 5 to the data. Middle panels: Simulated and experimental PO profiles at high H_2O ($[H_2O] = 6 \times 10^{15}$ (left-hand side) and $[H_2O] = 1 \times 10^{15}$ (right-hand side)). Bottom panels: Simulated and experimental PO profiles at zero H_2O. All left-hand panels are for experiments in N_2, while all right-hand panels are for experiments in He. Simulated fits which are considered good are (poor fits and reasons in brackets): Panel (c): red upward triangles (blue squares rise too fast, green diamonds loss too slow); Panel (d): red upward triangles (blue squares loss too slow, green diamonds rise too fast and loss too slow); Panel (e): red upward triangles (blue squares rise too fast); and Panel (f): red upward triangles and yellow downward triangles (blue squares loss too fast, green diamonds rise and loss too slow).

and to be comparable to the PO yields obtained from the numerical simulations (see Section 3.3), they were put on a relative scale by dividing the yield at each $[H_2O]$ by the yield at $[H_2O] = 0$. In this manner, all PO yield *vs* $[H_2O]$ plots start at 1 and are directly comparable. As can be seen from Fig. 5, the PO yields obtained using both N_2 and He as a bath gas increase with increasing $[H_2O]$, indicating P^* does indeed react with H_2O to produce PO.

3.3 Numerical simulations and determination of PO BRs

The PO product yields (γ) do not themselves give the BRs for PO formation from reactions R1 and R2. Instead, to determine the BR from the product yield, the other processes which remove P^* need to be accounted for. Table S2 gives the rate coefficients of the main reactions removing P^* in our experiments, together with the concentrations of the species employed in the experiments run with

Downloaded from https://academic.oup.com/mnras/article/515/1/99/6612737 by guest on 05 August 2022

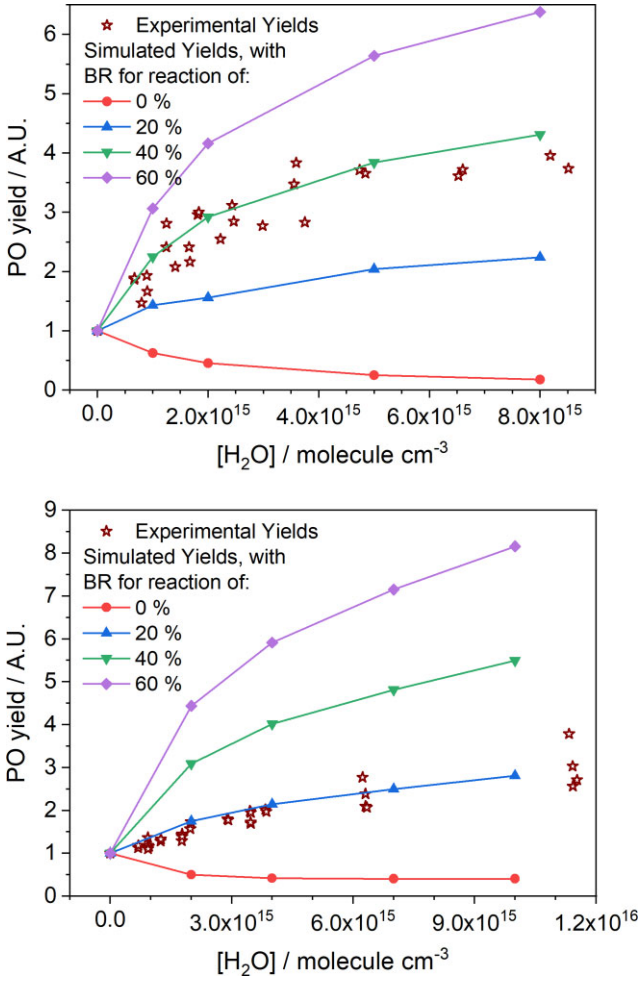

Figure 5. Experimental (open dark red stars) and simulated (closed symbols) PO yields. Top panel: experiments carried out in He, with model input parameters of $^2D/^2P$ = 2:1, $[O_2] = 1 \times 10^{14}$ cm^{-3}, O_2 BR = 100 %, $^4S{:}^2P$ = 0:1. Bottom panel: experiments carried out in N_2, with model input parameters of $^2D/^2P$ = 2:1, $[O_2] = 1 \times 10^{14}$ cm^{-3}, O_2 BR = 50 %, $^4S{:}^2P$ = 2:1.

either N_2 or He as a bath gas. When no H_2O was present in the reactor, P* could be removed by the PCl_3 precursor, any residual O_2, and in the case of P(^{2}D), any N_2 present. Knowing the concentrations of these species, the total first-order removal of each state of P* can be estimated, as well as the percentage of P* that is removed by each species. Assuming the reaction of P* with O_2 only produces PO (rather than relaxing the P*), we can assign the absolute PO yield observed in this experiment to the fraction of P* reacting with O_2 (this is 7.0 % for the experiments using N_2 bath gas, see Table S2). In an experiment, where H_2O is present, P* can now be removed by the PCl_3 precursor, the residual O_2, and the H_2O (and in the case of P(^{2}D), any N_2 present). Again, knowing the concentrations of these species we can determine the total first-order removal rate of each state of P*, and determine the percentage of P* that is removed by each species. In experiments using N_2 bath gas, and with an $[H_2O]$ of 1×10^{16} cm^{-3}, 0.9 % of the P* is removed by O_2, and 47.5 % by H_2O. If the removal of P* with H_2O proceeds only *via* the reactive channel producing PO, then 48.4 % of the P* will now go on to produce PO, compared with only 7.0 % when no H_2O is present. As such the absolute PO yield observed will be 6.9 times higher (47.5/7.0) at high H_2O compared to zero H_2O. Thus, by comparing the PO yield at various $[H_2O]$ relative to that with $[H_2O] = 0$, and knowing the percentage of P* that is being removed by H_2O and O_2, BRs for the reaction of P* with H_2O can be determined.

In practice, extracting a BR directly from the PO yields is complicated by several factors, which are discussed in the SI. Numerical simulations were therefore carried out using the numerical integration package Kintecus (Ianni 2003). PO profiles, over a range of $[H_2O]$ and for a range of P* + H_2O BRs, were simulated and fit using Equation E5, and simulated PO yields were obtained. These simulations were carried out over a range of input parameters as shown in Table 2. For a particular set of input parameters, the BR for PO production could be determined by comparing the simulated PO yields for a range of BRs to the experimentally determined yields. Fig. 5 compares the PO yields obtained when using N_2 and He as a bath gas with two sets of simulated yields. As can be seen, the input parameters used in the top panel ($^2D/^2P = 2{:}1$, $[O_2] = 1 \times 10^{14}$ cm^{-3}, O_2 BR = 100 per cent, $^4S{:}^2P = 0{:}1$) predict a BR of $\approx$ 35 per cent, while the input parameters in the bottom panel ($^2D/^2P = 2{:}1$, $[O_2] = 1 \times 10^{14}$ cm^{-3}, O_2 BR = 50 %, $^4S{:}^2P = 2{:}1$) predict a BR of $\approx$ 20 %. Varying the model input parameters over the ranges given in Table 2 resulted in the predicted BR ranging from around 5 to over 100 % (i.e. unphysical). However, many of the sets of input parameters could be ruled out by direct comparison of the simulated PO traces with the experimental traces. Fig. 4 compares experimental PO traces produced at high and zero $[H_2O]$ with simulated traces produced under the same conditions. If either the simulated high or zero H_2O trace produced for a particular set of model conditions did not match with the experimental trace, that set of conditions was ruled out. For example, in Fig. 4(e), the set of conditions that produced the PO trace shown by the blue squares clearly does not match the experimental PO trace, and as such, that particular set of conditions ($^2D/^2P = 2{:}1$, $[O_2] = 1 \times 10^{14}$ cm^{-3}, O_2 BR = 25 %, $^4S{:}^2P = 0{:}1$) can be ruled out. In this manner, we were able to discard many combinations of input parameters. Table 2 gives the final range of possible input parameters which were able to simulate satisfactorily the PO time-resolved traces and PO yields, indicating that the BR lies between 20 and 50%. We therefore quote the BRs for reactions R1 and R2 as (35 $\pm$ 15) %. See the SI for further details of the Kintecus model (Ianni 2003) and of how the full range of input parameters given in Table 2 were reduced.

4 DISCUSSION

4.1 Stellar optical excitation of P(^{4}S)

We have shown here that the excited P* states are much more reactive with H_2O and H_2 than ground-state P atoms. Similar behaviour was observed previously for the reactions of P* and P with O_2 (Douglas et al. 2019). The potential importance of optical excitation of P(^{4}S) in the stellar radiation field should therefore be considered. Although the optical transitions P($^4S_{3/2}$ $\rightarrow$ $^2D_{5/2}$) at 879 nm and P($^4S_{3/2}$ $\rightarrow$ $^2P_{1/2}$) at 534 nm are strongly forbidden with Einstein *A* coefficients of 2.0×10^{-4} and 4.3×10^{-2} s^{-1}, respectively (Kramida et al. 2021), the wavelengths at which these transitions occur are relatively close to the peak of the approximately blackbody emission curves from AGB stars with effective surface temperatures below 4000 K (Gustafsson et al. 2008).

The transition oscillator strengths (Kramida et al. 2021) can be used to calculate the following temperature-dependent absorption cross-sections (Okabe 1978): $\sigma(P(^4S_{3/2} - {}^2D_{5/2})) = 6.6 \times 10^{-23}$ $(T/1000)^{0.50}$ cm^2; $\sigma(P(^4S_{3/2} - {}^2D_{3/2})) = 4.4 \times 10^{-23}$ $(T/1000)^{0.50}$ cm^2; $\sigma(P(^4S_{3/2} - {}^2P_{1/2}) = 1.1 \times 10^{-21}$ $(T/1000)^{0.50}$ cm^2 and $\sigma(P(^4S_{3/2}$ -

Downloaded from https://academic.oup.com/mnras/article/515/1/99/6612737 by guest on 05 August 2022

Table 2. Ranges of input parameters were explored using Kintecus, and the possible ranges were found after ruling out those that did not match the experimental PO traces.

Input parameter	Range explored	Possible range
^{2}D:^{2}P Ratio	0.22–18	1–3
[O_2]/molecule cm^{-3}	0.5–3.0 × 10^{14}	1.0–1.5 × 10^{14}
BR for P* + O_2 → PO + O	25–100 %	50–100 %
^{4}S:^{2}P Ratio	0–18	0–2

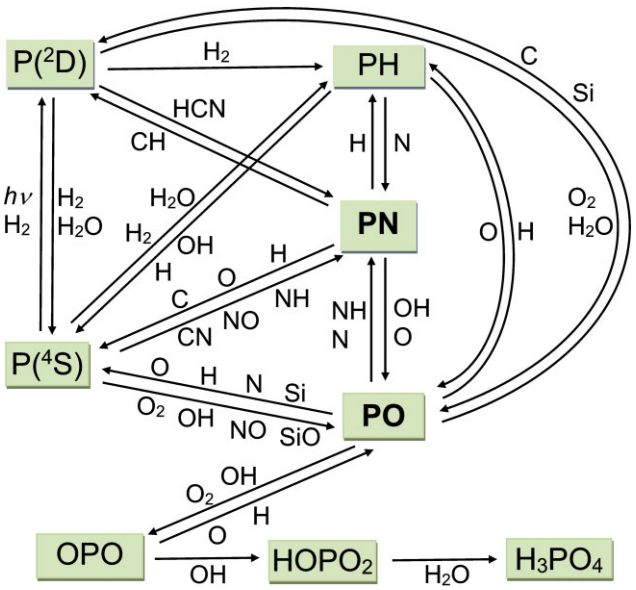

Figure 6. Schematic diagram of the phosphorus chemistry network developed in this study.

$^2P_{3/2}) = 5.3 \times 10^{-21}$ $(T/1000)^{0.50}$ cm^2. The stellar irradiance flux from the MARCS database (Gustafsson et al. 2008) for an evolved star with $T_* = 3300$ K indicates a photon flux at 879 nm of 3.0×10^{17} ph cm^{-2} s^{-1} nm^{-1} at 2R$_*$. Hence, the rate of optical excitation of P(^{4}S → ^{2}D) = 1.2×10^{-7} s^{-1}, corresponding to an e-folding time $\tau = 98$ days. The corresponding photon flux at 533 nm is 1.5×10^{17} ph cm^{-2} s^{-1} nm^{-1} at 2R$_*$, so the P(^{4}S → ^{2}P) rate of excitation = 2.08×10^{-6} s^{-1}, with $\tau = 5.6$ d. These rates are compared with collisional energy transfer rates in the next section.

4.2 A new chemical network for Phosphorus

In this section, we describe the development of the phosphorus chemistry network which is illustrated schematically in Fig. 6. Table 3 lists the reactions in the network, along with the rate coefficients and a note of their source. In addition to the experimental results from this study, we have previously measured a number of other rate coefficients for reactions involving P-bearing species (Douglas et al. 2019; 2020). In order to estimate rate coefficients for reactions that have not been studied experimentally, we have used electronic structure theory at the CBS-QB3 level (Montgomery et al. 2000, Frisch et al. 2016) to determine the stationary points on the relevant reaction potential energy surfaces, combined with the Master Equation Solver for Multi-Energy well Reactions (MESMER) program (Glowacki et al. 2012). The use of these theoretical approaches is described in detail in the SI, along with notes on individual reactions. This approach should represent a significant improvement in our earlier study (Gobrecht et al. 2016), where rate coefficients for P-bearing species were set to their N analogues. In general, the new rate coefficients are within an order of magnitude of those assuming N↔P isovalence.

The rate coefficient for collisional excitation of P(^{4}S) to P(^{2}D) (k_{-21} in Table 3), shows that at a temperature of 1500 K and [H_2] = 10^{11} cm^{-3} (i.e. typical values around 2R$_*$ in an outflow), the lifetime for collisional excitation is $1/(k_{-21}\,[H_2]) \sim 4300$ s. This is 1950 times shorter than the optical pumping lifetime of 98 d (Section 4.1), and so optical excitation of P(^{4}S → ^{2}D) will not be significant in the inner stellar wind. In contrast, collisional excitation of P(^{4}S) to P(^{2}P) will occur with an e-folding lifetime of 37 d under the same conditions, which is significantly longer than the optical pumping lifetime of 5.6 d (Section 4.1). Nevertheless, since collisional excitation of P(^{4}S) to P(^{2}D) is 110 times faster than optical pumping to P(^{2}P), the role of P(^{2}P) should be very limited in this environment, and so reactions involving P(^{2}P) are not included in the chemistry network (Table 3).

In the experiments on P(^{2}D) + H_2, although we measured the temperature-dependent rate coefficient for the removal of P(^{2}D), it was not possible to determine whether physical quenching to P(^{4}S) or reaction to PH + H was occurring. The measured activation energy is 5.8 ± 0.2 kJ mol^{-1}. Calculations we performed at the very accurate W1BD level of theory (Barnes et al. 2009, Frisch et al. 2016) show that the reaction P(^{2}D) + H_2 → PH + H is endothermic by 3.3 kJ mol^{-1}, which accords with the measured activation energy (within the expected error of 4 kJ mol^{-1} at this level of theory). However, we also find that there is a barrier of 16 kJ mol^{-1} on the doublet potential energy surface for the reaction. This barrier is significantly larger than the measured activation energy, which is good evidence that physical (i.e. collisional) quenching, rather than reaction, remove P(^{2}D) in the presence of H_2. Nevertheless, as a sensitivity study in the stellar outflow modelling described in the next section, we treated unreactive and reactive collisions between P and H_2 as two extreme cases: The more likely *Scenario 1*, where P(^{2}D) + H_2 → P(^{4}S) + H_2 and the reverse reaction are unreactive (reactions 21 and –21 in Table 3); or *Scenario 2*, where P(^{2}D) + H_2 → PH + H, P(^{4}S) + H_2 → PH + H and the reverse PH + H → P(^{4}S) + H_2 are reactive (reactions 21', 22', and –22' in Table 3).

Lastly, we include in the network the formation of $HOPO_2$ and H_3PO_4 (phosphoric acid). The rate coefficients for the reactions which form these species (R19 and R20 in Table 3) are taken from a model that we developed recently to describe phosphorus chemistry in planetary atmospheres, where phosphate is a very stable sink for P produced by meteoric ablation (Plane et al. 2021).

4.3 Numerical modelling

We use here a model that we applied recently to circumstellar gas trajectories, including non-pulsating and pulsating outflows, for two late-type stars with a different evolutionary stage: a semi-regular (SRV) AGB star, and a Mira-type (MIRA) AGB star (Gobrecht et al. 2022). In this study, we use the gas trajectories of the MIRA model star in oxygen-rich conditions (C/O = 0.75), characterized

Downloaded from https://academic.oup.com/mnras/article/515/1/99/6612737 by guest on 05 August 2022

Table 3. Reactions and rate coefficients in the Phosphorus chemical network.

	Reaction	Rate coefficient[a]	Notes
1	$P + O_2 \rightarrow PO + O$	4.2×10^{-12} exp(–600/*T*)	Douglas et al. (2019)
–1	$PO + O \rightarrow P + O_2$	1.8×10^{-13} (*T*/300)$^{0.79}$ exp(–10 054/*T*)	Detailed balance with R1
2	$PO + O_2 \rightarrow OPO + O$	2.3×10^{-11} exp(–100/*T*)	(Douglas et al. 2020)
–2	$OPO + O \rightarrow PO + O_2$	3.5×10^{-11} exp(–1449/*T*)	Detailed balance with R2
3	$P + NO \rightarrow PN + O$	7.1×10^{-11} exp(–6427/*T*)	MESMER calculation[b]
–3	$PN + O \rightarrow P + NO$	1.0×10^{-10} exp(–3158/*T*)	MESMER calculation[b]
4	$P + OH \rightarrow PO + H$	6.9×10^{-12} (*T*/300)$^{-0.29}$	Trajectory calculation[b]
–4	$PO + H \rightarrow P + OH$	4.2×10^{-13} (*T*/300)$^{0.82}$ exp(–16 791/*T*)	Detailed balance with R4
5	$P + H_2O \rightarrow PH + OH$	9.0×10^{-10} exp(–24 319/*T*)	Detailed balance with R-5
–5	$PH + OH \rightarrow P + H_2O$	1.0×10^{-10} (*T*/300)$^{0.167}$	Collision capture rate[b]
6	$PO + N \rightarrow P + NO$	5.5×10^{-11} exp(–12 869/*T*)	MESMER calculation[b]
–6	$P + NO \rightarrow PO + N$	1.0×10^{-10} exp(-17 056/*T*)	MESMER calculation[b]
7	$PO + N \rightarrow PN + O$	9.8×10^{-11} exp(175/*T*)	MESMER calculation[b]
–7	$PN + O \rightarrow PO + N$	2.7×10^{-10} exp(–744/*T*)	MESMER calculation[b]
8	$PH + O \rightarrow PO + H$	2.0×10^{-10}	Collision capture rate[b]
–8	$PO + H \rightarrow PH + O$	2.8×10^{-10} (T/300)$^{0.26}$ exp(–34 462/*T*)	Detailed balance with R8
9	$PN + OH \rightarrow PO + NH$	2.6×10^{-10} exp(–13 002/*T*)	Detailed balance with R-9
–9	$PO + NH \rightarrow PN + OH$	1.0×10^{-10}	Collision capture rate[b]
10	$P + NH \rightarrow PN + H$	3.0×10^{-10}	Collision capture rate[b]
–10	$PN + H \rightarrow P + NH$	4.3×10^{-12} (*T*/300)$^{1.19}$ exp(–27 868/*T*)	MESMER calculation[b]
11	$PN + CH \rightarrow HCN + P(^2D)$	1.0×10^{-10}	Collision capture rate[b]
–11	$HCN + P(^2D) \rightarrow PN + CH$	1.0×10^{-10} exp(–39 200)	Detailed balance with R11
12	$PN + C \rightarrow CN + P$	1.1×10^{-10}	Collision capture rate[b]
–12	$P + CN \rightarrow PN + C$	7.3×10^{-10} exp(–16 240)	Detailed balance with R12
13	$PO + C \rightarrow P(^2D) + CO$	5.0×10^{-11}	See the SI[b]
14a	$PO + Si \rightarrow P + SiO$	2.1×10^{-10} (*T*/300)$^{0.10}$	MESMER calculation[b]
14b	$PO + Si \rightarrow P(^2D) + SiO$	2.1×10^{-10} (*T*/300)$^{0.01}$	MESMER calculation[b]
–14a	$P + SiO \rightarrow PO + Si$	3.5×10^{-10} exp(24 416/*T*)	MESMER calculation[b]
15	$PH + N \rightarrow PN + H$	1.0×10^{-10} (*T*/300)$^{0.17}$	MESMER calculation[b]
–15	$PN + H \rightarrow PH + N$	3.1×10^{-10} (*T*/300)$^{0.51}$ exp(–35 427/*T*)	MESMER calculation[b]
16	$PO + OH \rightarrow OPO + H$	1.2×10^{-10}	Collision capture rate[b]
–16	$OPO + H \rightarrow PO + OH$	1.0×10^{-9} exp(–9490/*T*)	Detailed balance with R-16
17a	$P(^2D) + H_2O \rightarrow PO + H_2$	1.6×10^{-11}	This study (reaction 2a[c])
17b	$P(^2D) + H_2O \rightarrow P + H_2O$	3.0×10^{-11}	This study (reaction 2b[c])
18	$P(^2D) + O_2 \rightarrow PO + O$	1.2×10^{-11} (*T*/300)$^{0.82}$ exp(177/*T*)	Douglas et al. (2019)
19	$OPO + OH (+ H_2) \rightarrow HOPO_2$	2.2×10^{-26} (*T*/300)$^{-5.25}$	Plane et al. (2021)
20	$HOPO_2 + H_2O (+ H_2) \rightarrow H_3PO_4$	3.0×10^{-26} (*T*/300)$^{-7.53}$	Plane et al. (2021)
		Scenario 1	
21	$P(^2D) + H_2 \rightarrow P + H_2$	8.0×10^{-11} exp(-699/*T*)	This study (reaction R4b[c])
–21	$P + H_2 \rightarrow P(^2D) + H_2$	2.0×10^{-10} exp(–17 056/*T*)	Detailed balance with R21
		Scenario 2	
21'	$P(^2D) + H_2 \rightarrow PH + H$	8.0×10^{-11} exp(-699/*T*)	This study (reaction R4a[c])
22'	$P + H_2 \rightarrow PH + H$	6.7×10^{-10} exp(–17 349/*T*)	Transition state theory[b]
–22'	$PH + H \rightarrow P + H_2$	6.7×10^{-11} exp(–346/*T*)	Detailed balance with R22'

[a]Units: cm^3 molecule^{-1} s^{-1} for bimolecular reactions; cm^6 molecule^{-2} s^{-1} for termolecular reactions.
[b]See the supporting information for further details.
[c]Reaction number in the text.

by a total density of $n_{gas} = 4 \times 10^{14}$ cm^{-3} and a temperature of 2000 K at the stellar surface. The phosphorus chemistry in Table 3 was added to the oxygen-rich kinetic network in the model. The resulting model outputs are illustrated in Fig. 7. Note that because the recombination reaction R20 of $HOPO_2$ with H_2O is much faster than the recombination R19 of OPO with OH (since [H_2O] >> [OH]), $HOPO_2$ is rapidly converted into H_3PO_4 and, for reasons of clarity, this latter species is not shown in the panels in Fig. 7. The total gas density, temperature and fractional abundances of species in the outflow which impact on the phosphorus chemistry (H, H_2, H_2O, OH, O, O_2, N, and N_2) are listed in Table S5 in the SI.

In the non-pulsating case (Fig. 7a), the time for the outflow to reach 1.5 R_* is 377 d, and 551 d to reach 2 R_*. The corresponding conditions in the gas are $n_{gas} = 5.8 \times 10^{12}$ cm^{-3} and $T = 1570$ K at 1.5 R_* and 4.31×10^{11} cm^{-3} and 1320 K at 2.0 R_*. In this case, the phosphorus chemistry is dominated by PO, which is mainly formed by the barrierless reactions P + OH (R4) and $P(^2D) + H_2O$ (R17a). This is because in the hot region OH has a relatively high concentration, and the $P(^2D)/P(^4S)$ ratio is favoured by collisional

Downloaded from https://academic.oup.com/mnras/article/515/1/99/6612737 by guest on 05 August 2022

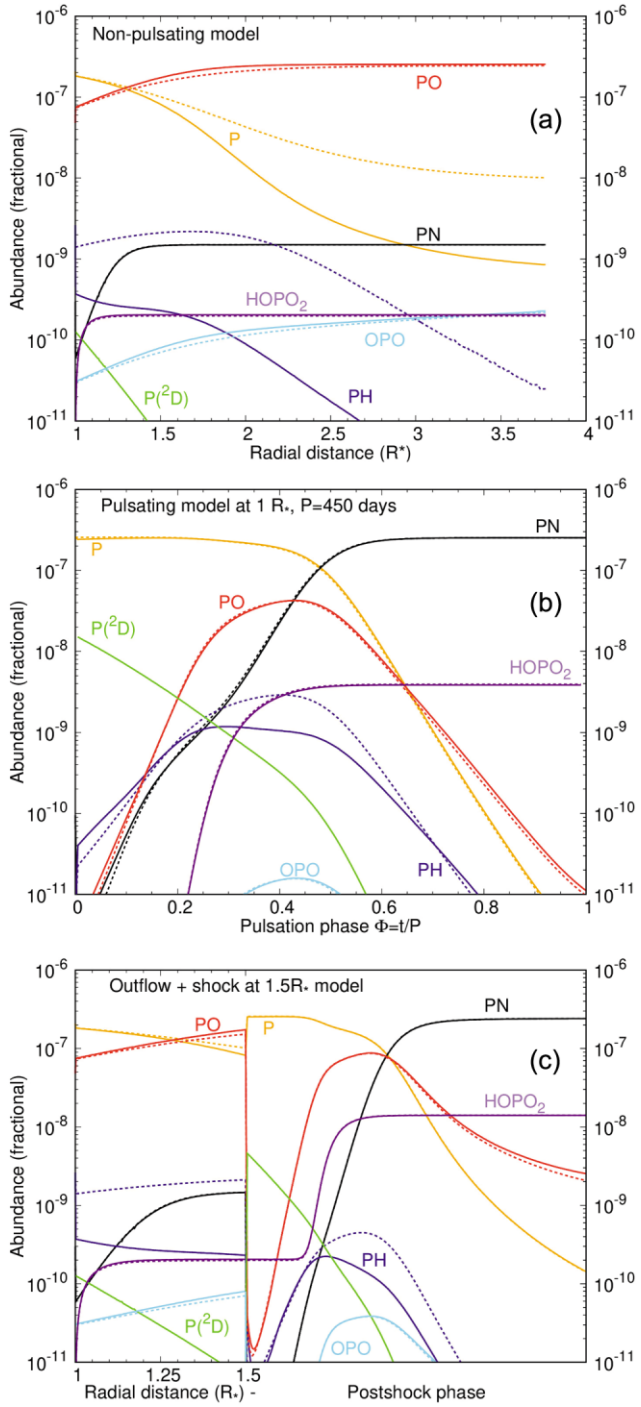

Figure 7. Molecular abundances of the P-bearing species in the different stellar outflow models: Panel (a) – a non-pulsating, steady outflow with a monotonically increasing radial distance from the star, corresponding to decreasing gas densities, and temperatures; Panel (b): the post-shock gas of a pulsating outflow that experiences a shock at 1 R∗ and relaxes to its preshock condition within one pulsation period; Panel (c): a combination of a steady outflow (from 1.0–1.5 R_*) and a subsequent pulsational shock at 1.5 R_*, including the related post-shock gas. Solid lines correspond to Scenario 1 and dashed lines to Scenario 2 (see the text). Note that $HOPO_2$ is rapidly converted into H_3PO_4, and so the latter is not shown for clarity.

excitation of P(^{4}S) by H_2 (reaction R21). The reaction of P with O_2 (R1) is of secondary importance because of the low O_2 density in the inner wind of the outflow.

Although the predicted PO fractional abundance greater than 10^{-7} is a dramatic improvement on our previous model (where PO was underpredicted by around 3 orders of magnitude (Gobrecht et al. 2016)), in this non-pulsating model the PN abundance is just over 10^{-9}, which is roughly 2 orders of magnitude lower than observed (see Section 1). Moreover, only small amounts of OPO and $HOPO_2$ are simulated, so the formation of the potential biomolecule H_3PO_4 is limited. Scenario 2 makes very little difference to PO and PN, though there is a significant increase in PH and a decrease in P(^{2}D), as expected when collisions between P(^{2}D and ^{4}S) with H_2 are treated as being reactive (Table 3).

In the pulsating model (Fig. 7b), the hydrodynamical time-scale is set by the pulsation period of 450 d and corresponds to the time for the non-pulsating outflow to reach a radial position between 1.5 and 2 R_*. We assume that the stellar pulsation steepens into a shock wave at the stellar surface. The immediate post-shock conditions are very hot and dense ($n_{gas} = 6.8 \times 10^{15}$ cm^{-3} and $T = 4480$ K). In this case, PN represents the most abundant phosphorus-bearing molecule for phases $\Phi > 0.5$ in the model. However, the abundance of PO does not persist in the pulsating model at 1 R_*, and is comparable to observations only when Φ lies between 0.25 and 0.55.

The difference in the phosphorus chemistry between the non-pulsating and pulsating models arises because, in the hotter and denser pulsating model, a much larger fraction of molecular N_2 becomes thermally dissociated:

$$N_2 + M \rightarrow N + N + M\,(M = H_2, H, He, \text{etc.})\,, \qquad \text{(R23)}$$

where R23 has a substantial activation energy: $k_{23} = 9.2 \times 10^{-5} (T/298)^{-2.50} \exp(-113060/T)$ cm^3 molecule^{-1} s^{-1} (Kewley & Hornung 1974). PO can then react with atomic N to form PN via reaction R7 (Table 3). This reaction is close to thermoneutral ($\Delta H^\circ_{(0\,K)} = -7$ kJ mol^{-1}), so the PO/PN ratio is largely controlled by the O/N ratio. In the cooler non-pulsating model, R23 is very slow and the O/N ratio is therefore larger.

Interestingly, a significant quantity of $HOPO_2$ (and H_3PO_4) forms, with the fractional abundance of 4×10^{-9} exceeding the corresponding abundance of the non-pulsating model by factor of ∼20. This arises because of a 20-fold increase in O_2 after the shock (Table S5), which favours the conversion of PO into OPO (R2); significant reductions early in the pulsation cycle ($\Phi > 0.2$) in O and H, which destroy OPO (R-2 and R-16); and the 15-fold increase in total gas density which favours the termolecular recombination of OPO with OH to form $HOPO_2$.

As a final modelling step, we combine the non-pulsating and the pulsating model by assuming a monotonic outflow from the stellar surface (1 R_*) out to 1.5 R_* ($n_{gas} = 5.8 \times 10$ cm^{-3} and $T = 1570$ K), followed by a pulsation-induced shock. This results in immediate post-shock conditions of $n_{gas} = 3.8 \times 10^{13}$ cm^{-3} and $T = 3360$ K at 1.5 R_*, which then relaxes over the time-scale of the pulsation period. In the post-shock gas model the PO and PN abundances are around 10^{-7} for the intermediate phases (see Fig. 7c). At full phase ($\Phi \rightarrow 1$), the PO abundance ($\sim 2 \times 10^{-9}$) is rather low, but still orders of magnitude higher than in the pulsating model at 1 R_*. The model therefore confirms earlier work (e.g. Lefloch et al. 2016; Mininni et al. 2018), which proposed that high PN levels form in the shocked regions of astrophysical outflows. This probably at least partially explains why the PO/PN ratios observed around different stars are quite variable (see Section 1). A final point of note is that in this

Downloaded from https://academic.oup.com/mnras/article/515/1/99/6612737 by guest on 05 August 2022

model run H_3PO_4 (or $HOPO_2$) forms effectively in the post-shock gas and reaches abundances above 10^{-8}.

5 CONCLUSIONS

In this study of phosphorus chemistry in stellar outflows, we first investigated the role of excited P atom chemistry in producing PO from the reaction of the low-lying metastable P(^{2}D) and P(^{2}P) states with H_2O. The measured rate coefficients of both reactions are reasonably fast, with a PO yield of ∼35 %. H_2 was shown to react with both P states relatively efficiently, with physical quenching, rather than chemical reaction to produce PH + H, being the more likely pathway for P(^{2}D) + H_2. We then developed a comprehensive phosphorus chemistry network for inclusion in a stellar outflow model, using a combination of electronic structure theory calculations and a Master Equation treatment of reactions taking place over complex potential energy surfaces. The new model shows that at high temperatures within ∼2 stellar radii, collisional excitation of ground-state P(^{4}S) to P(^{2}D), followed by reaction with H_2O, is a significant pathway for producing PO, along with the reaction between P(^{4}S) and OH. The model also demonstrates that the PN fractional abundance in a steady (non-pulsating) outflow is underpredicted by about 2 orders of magnitude compared with observation. However, under shocked conditions where enough thermal dissociation of N_2 occurs at temperatures above 4000 K, the resulting N atoms convert a substantial fraction of PO into PN, which is consistent with reports that PN tends to correlate in some (often carbon-rich) environments with the shock tracer SiO.

ACKNOWLEDGEMENTS

This study was supported by funding from the UK Science and Technology Facilities Council (grant ST/P000517/1). DG was funded by the project grant 'The Origin and Fate of Dust in Our Universe' from the Knut and Alice Wallenberg Foundation.

Note added in proof. It has come to our attention that a very recent paper [J. G. de la Concepción, C. Puzzarini, V. Barone, I. Jiménez-Serra, O. Roncero, 2021, Astrophys. J., 922, 169] describes a theoretical study of the reactions of P(^{4}S, ^{2}D and ^{2}P) with OH and H_2O, concluding that these are important sources of PO in the cold interstellar medium (complementing the work of the present study on P chemistry in hot circumstellar environments). The measured rate coefficients in the present study for P(^{2}P) + H_2O is around 50 times slower in the 300 – 400 K temperature range than that calculated by Concepción et al. (2021).

DATA AVAILABILITY

All the experimental and modelling data is included in Tables in the main paper or the Supporting Information.

REFERENCES

Acuña A. U., Husain D., Wiesenfeld J. R., 1973, J. Chem. Phys., 58, 494
Asplund M., Grevesse N., Sauval A. J., Scott P., 2009, in Blandford R., Kormendy J., van Dishoeck E., eds., Ann. Rev. Astron. Astrophys. Annual Rev., Palo Alto, p. 481
Barnes E. C., Petersson G. A. J. A. M., Jr., Frisch M. J., Martin J. M. L., 2009, J. Chem. Theory Comput., 5, 2687
Bernal J. J., Koelemay L. A., Ziurys L. M., 2021, ApJ, 906, 55
Bridgeman O. C., Aldrich E. W., 1964, J. Heat Transfer, 86, 279
Chantzos J., Rivilla V. M., Vasyunin A., Redaelli E., Bizzocchi L., Fontani F., Caselli P., 2020, A&A, 633, A54
De Beck E., Kamiński T., Patel N. A., Young K. H., Gottlieb C. A., Menten K. M., Decin L., 2013, A&A, 558, A132
Douglas K. M., Blitz M. A., Mangan T. P., Plane J. M. C., 2019, J. Phys. Chem. A, 123, 9469
Douglas K. M., Blitz M. A., Mangan T. P., Western C. M., Plane J. M. C., 2020, J. Phys. Chem. A, 124, 7911
Fontani F., Rivilla V. M., van der Tak F. F. S., Mininni C., Beltran M. T., Caselli P., 2019, MNRAS, 489, 4530
Frisch M. J. et al., 2016, Gaussian, Inc., Wallingford, CT
Glowacki D. R., Liang C.-H., Morley C., Pilling M. J., Robertson S. H., 2012, J. Phys. Chem. A, 116, 9545
Gobrecht D., Cherchneff I., Sarangi A., Plane J. M. C., Bromley S. T., 2016, A&A, 585, A6
Gobrecht D., Plane J. M. C., Bromley S. T., Decin L., Cristallo S., Sekaran S., 2022, A&A, 658, A167
Gómez Martín J. C., Blitz M. A., Plane J. M. C., 2009, Phys. Chem. Chem. Phys., 11, 671
Gustafsson B., Edvardsson B., Eriksson K., Jørgensen U. G., Nordlund Å., Plez B., 2008, A&A, 486, 951
Ianni J. C., 2003, in Bathe K.J.ed., Computational Fluid and Solid Mechanics. Elsevier Science Ltd., Oxford
Jimenez-Serra I., Viti S., Quenard D., Holdship J., 2018, ApJ, 862, 128
Kewley D. J., Hornung H. G., 1974, Chem. Phys. Lett., 25, 531
Kramida A., Ralchenko Y., Reader J., 2021, NIST Atomic Spectra Database (version 5.9). National Institute of Standards and Technology, Gaithersburg, MD.
Lefloch B. et al., 2016, MNRAS, 462, 3937
Mangan T. P., McAdam N., Daly S. M., Plane J. M. C., 2019, J. Phys. Chem. A, 123, 601
Mininni C., Fontani F., Rivilla V. M., Beltran M. T., Caselli P., Vasyunin A., 2018, MNRAS, 476, L39
Molpeceres G., Kästner J., 2021, ApJ, 910, 55
Montgomery J. A., Frisch M. J., Ochterski J. W., Petersson G. A., 2000, J. Chem. Phys., 112, 6532
Okabe H., 1978, Photochemistry of Small Molecules. John Wiley & Sons, New York, NY
Plane J. M. C., Feng W. H., Douglas K. M., 2021, J. Geophys. Res.-Space Phys., 126, e2021JA029881
Rivilla V. M. et al., 2018, MNRAS, 475, L30
Sausa R. C., Miziolek A. W., Long S. R., 1986, J. Phys. Chem., 90, 3994
Schwartz A. W., 2006, Phil. Trans. R. Soc. B, 361, 1743
Sil M. et al., 2021, AJ, 162, 119
Souza A. C., Silva M. X., Galvao B. R. L., 2021, MNRAS, 507, 1899
Velilla Prieto L. et al., 2017, A&A, 597, A25
Walton C. R. et al., 2021, Earth Sci. Rev., 221
Williams D. A., Hartquist T. W., 2013, The Cosmic-Chemical Bond: Chemistry from the Big Bang to Planet Formation. Royal Society of Chemistry, Cambridge
Ziurys L. M., Schmidt D. R., Bernal J. J., 2018, ApJ, 856, 169

SUPPORTING INFORMATION

Supplementary data are available at *MNRAS* online.

Supplementary Information v3.docx

Please note: Oxford University Press is not responsible for the content or functionality of any supporting materials supplied by the authors. Any queries (other than missing material) should be directed to the corresponding author for the article.

This paper has been typeset from a TEX/LATEX file prepared by the author.

Downloaded from https://academic.oup.com/mnras/article/515/1/99/6612737 by guest on 05 August 2022